High-Yield Gas−Liquid Interfacial Synthesis of Highly Dispersed Fe₃O₄ Nanocrystals and Their Application in Lithium-Ion Batteries

Zhi-Min Cui,[†] Ling-Yan Jiang,[†] Wei-Guo Song,* and Yu-Guo Guo*

Laboratory of Molecular Nanostructures and Nanotechnology, Institute of Chemistry, Chinese Academy of Sciences, Beijing 100190, People's Republic of China, and Beijing National Laboratory for Molecular Sciences (BNLMS), Beijing 100190, People's Republic of China

A beaker-in-autoclave setup is designed for interfacial synthesis of Fe₃O₄ nanoparticles with precise size control. They exhibit superparamagnetic properties and can be homogeneously incorporated into a carbon matrix to form Fe₃O₄@C composite, in which Fe₃O₄ remains highly dispersed in the solid state. The Fe₃O₄@C composites exhibit excellent cycling and rate performances as anode material for lithium-ion batteries.

Introduction

Magnetite (Fe₃O₄) nanoparticles are very useful in bio-analysis, ferrofluids, magnetic resonance imaging, and Li$^+$-ion-battery applications.[1−8] Most of these applications require that the Fe₃O₄ nanoparticles to be chemically stable, uniform in size, and well-dispersed in liquid media, preferably in water. Important progress has been made in the chemical synthesis of Fe₃O₄ nanoparticles. Methods including coprecipitation, hydrothermal method, the reverse micelle method, laser pyrolysis techniques, thermal decomposition of iron oleate, etc. have been used to synthesize highly dispersed magnetite nanoparticles.[9−13] For example, Li et al. developed a thermal decomposition method to synthesize water-soluble Fe₃O₄ nanocrystals using FeCl₃ as the iron source and 2-pyrrolidone as the solvent under reflux (245 °C).[14,15] However, in these methods, toxic and/or expensive precursors are often used, as well as high-boiling-point organic solvents, and the reactions are usually conducted at high temperature. The nanoparticles obtained are usually dispersible only in organic solvents. To be soluble in the aqueous phase, the nanoparticles must be capped with functional groups.[16−18]

Nanosized transition-metal oxides, including Fe₃O₄ nanoparticles, have been demonstrated to be promising anode materials with high capacity for lithium-ion batteries.[19−22] However, the poor cycling performance of Fe₃O₄ is delaying its practical application. This problem can be partially solved by intentionally mixing Fe₃O₄ with particular nanostructures, for example, by loading iron oxide onto carbon as an Fe₃O₄/C composite.[23] To further improve the performance of Fe₃O₄ as anode materials in lithium-ion batteries, Fe₃O₄/C composite with rationally designed nanostructure is necessary.[8,24]

In this paper, we designed a gas−liquid interfacial route to synthesize water-soluble, highly dispersed magnetic nanoparticles. In this "beaker-in-autoclave" method, relatively inexpensive and environmental benign chemicals such as iron nitrate and ethylene glycol (EG) and ammonia solution are used. The method is reliable and inexpensive, and the yield

* Author to whom correspondence should be addressed. Tel./Fax: (+86)10-62557908. E-mail: wsong@iccas.ac.cn.
† Also with the Graduate School of the Chinese Academy of Sciences, Beijing 100049, PRC.

(1) Sun, C.; Veiseh, O.; Gunn, J.; Fang, C.; Hansen, S.; Lee, D.; Sze, R.; Ellenbogen, R. G.; Olson, J.; Zhang, M. *Small* **2008**, *4*, 372.
(2) Gupta, A. K.; Naregalkar, R. R.; Vaidya, V. D.; Gupta, M. *Nanomedicine* **2007**, *2*, 23.
(3) Xu, C. J.; Sun, S. H. *Polym. Int.* **2007**, *56*, 821.
(4) Moser, A.; Takano, K.; Margulies, D. T.; Albrecht, M.; Sonobe, Y.; Ikeda, Y.; Sun, S. H.; Fullerton, E. E. *J. Phys. D: Appl. Phys.* **2002**, *35*, R157.
(5) Hultman, K. L.; Raffo, A. J.; Grzenda, A. L.; Harris, P. E.; Brown, T. R.; O'Brien, S. *ACS Nano* **2008**, *2*, 477.
(6) Lu, A. H.; Salabas, E. L.; Schuth, F. *Angew. Chem., Int. Ed.* **2007**, *46*, 1222.
(7) Banov, B.; Ljutzkanov, L.; Dimitrov, I.; Trifonova, A.; Vasilchina, H.; Aleksandrova, A.; Mochilov, A.; Hang, B. T.; Okada, S.; Yamaki, J. I. *J. Nanosci. Nanotechnol.* **2008**, *8*, 591.
(8) Zhang, W. M.; Wu, X. L.; Hu, J. S.; Guo, Y. G.; Wan, L. J. *Adv. Funct. Mater.* **2008**, *18*, 1.
(9) Zhang, Y. H.; Chen, S. M.; Chen, J. H.; Xiong, H. B.; Zhang, Q. W.; Shen, H.; Gong, K. C. *Chem. J. Chin. Univ.−Chin.* **2003**, *24*, 1717.
(10) Park, J.; Joo, J.; Kwon, S. G.; Jang, Y.; Hyeon, T. *Angew. Chem., Int. Ed.* **2007**, *46*, 4630.
(11) Wang, X.; Zhuang, J.; Peng, Q.; Li, Y. D. *Nature* **2005**, *437*, 121.
(12) Osaka, T.; Matsunaga, T.; Nakanishi, T.; Arakaki, A.; Niwa, D.; Iida, H. *Anal. Bioanal. Chem.* **2006**, *384*, 593.
(13) Morales, M. P.; Bomati-Miguel, O.; de Alejo, R. P.; Ruiz-Cabello, J.; Veintemillas-Verdaguer, S.; O'Grady, K. *J. Magn. Magn. Mater.* **2003**, *266*, 102.

(14) Li, Z.; Sun, Q.; Gao, M. Y. *Angew. Chem., Int. Ed.* **2005**, *44*, 123.
(15) Li, Z.; Chen, H.; Bao, H. B.; Gao, M. Y. *Chem. Mater.* **2004**, *16*, 1391.
(16) De Palma, R.; Peeters, S.; Van Bael, M. J.; Van den Rul, H.; Bonroy, K.; Laureyn, W.; Mullens, J.; Borghs, G.; Maes, G. *Chem. Mater.* **2007**, *19*, 1821.
(17) Chen, Z. P.; Zhang, Y.; Zhang, S.; Xia, J. G.; Liu, J. W.; Xu, K.; Gu, N. *Colloid Surf., A* **2008**, *316*, 210.
(18) Latham, A. H.; Williams, M. E. *Acc. Chem. Res.* **2008**, *41*, 411.
(19) Poizot, P.; Laruelle, S.; Grugeon, S.; Dupont, L.; Tarascon, J. M. *Nature* **2000**, *407*, 496.
(20) Zheng, S. F.; Hu, J. S.; Zhong, L. S.; Song, W. G.; Wan, L. J.; Guo, Y. G. *Chem. Mater.* **2008**, *20*, 3617.
(21) Cao, A. M.; Hu, J. S.; Liang, H. P.; Wan, L. J. *Angew. Chem., Int. Ed.* **2005**, *44*, 4391.
(22) Taberna, L.; Mitra, S.; Poizot, P.; Simon, P.; Tarascon, J. M. *Nat. Mater.* **2006**, *5*, 567.
(23) Hang, B. T.; Watanabe, I.; Doi, T.; Okada, S.; Yamaki, J. I. *J. Power Sources* **2006**, *161*, 1281.
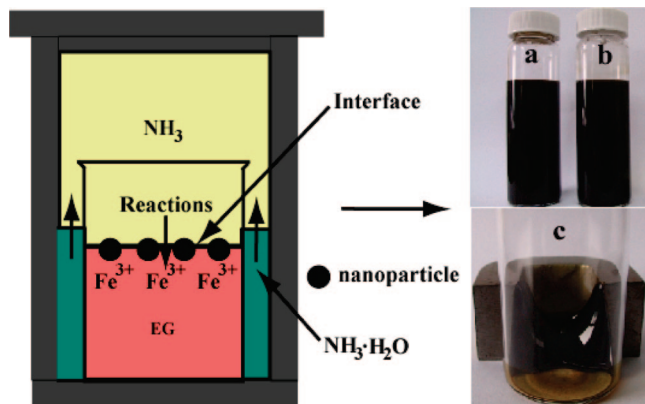(24) Wang, L.; Yu, Y.; Chen, P. C.; Zhang, D. W.; Chen, C. H. *J. Power Sources* **2008**, *183*, 717.

Figure 1. Schematic illustration for the reaction system and digital photograph for the as-synthesized product dispersed (7.0 mg/mL) in ethanol (vial a) and water (vial b). Panel c shows a photograph image of the concentrated ethanol solution (50 mg/mL) in the presence of a magnet.

against iron nitrate is almost 100%. The Fe_3O_4 nanoparticles are superparamagnetic and water-soluble. Furthermore, the Fe_3O_4 nanoparticles can be incorporated into a carbon matrix through a simple hydrothermal method to form $Fe_3O_4@C$ composite. In the $Fe_3O_4@C$ composite, Fe_3O_4 nanoparticles remain dispersed in a carbon matrix. This novel nanostructure allows $Fe_3O_4@C$ composites to be excellent anode materials for high-performance Li^+-ion batteries.

Experimental Section

Materials and Reagents. Ethylene glycol (EG), $Fe(NO_3)_3 \cdot 9H_2O$, ethanol, glucose, tetraethylorthosilicate (TEOS), and ammonia solution (concentration of 25 wt %) were purchased from Beijing Chemical Reagent Co. All chemicals were used as received, without further purification.

Synthesis of Highly Dispersed Magnetite Nanocrystals. As shown in Figure 1, in a 15-mL beaker, 0.404 g of $Fe(NO_3)_3 \cdot 9H_2O$ was dissolved in 5 mL of EG. The beaker was placed into a 30-mL Teflon-lined autoclave that contained 6 mL of an ammonia solution. The autoclave then was sealed and placed in a programmable microwave oven (MDS-6, Shanghai Sino Microwave Chemistry Technology Co., Ltd.). The oven was heated to 170 °C by microwave irradiation in 1 min and then kept at that temperature for various times (10 min, 1 h, or 3 h). After cooling and centrifugation and washing with ethanol for several times, a dark powder was collected, which was redispersed in ethanol to form a 7.0 mg/mL solution for further tests.

Encapsulation of the Highly Dispersed Nanoparticles. In the silica encapsulation experiment, the Stöber method was applied, with minor modification.[25] A hydrothermal method was applied in the carbon incorporating process.[26] In a typical experiment, 1.5 g of glucose was dissolved in a mixture of 9.0 mL of deionized water and 6.0 mL of ethanol. Then, 120.0 mg of Fe_3O_4 nanoparticles (which is the product after a reaction time of 1 h) was added, followed by ultrasonic irradiation for 30 min. The solution was sealed in a 50-mL Teflon-lined autoclave and heated at 190 °C for 15 h. The dark brown products were washed and separated by centrifugation−redispersion cycles with deionized water and dried under vacuum at 100 °C. For the Li^+-ion battery tests, the dried products were calcined at 600 °C for 20 h under a nitrogen flow.

(25) Lu, Y.; Yin, Y. D.; Mayers, B. T.; Xia, Y. N. *Nano Lett.* **2002**, *2*, 183.
(26) Zhang, W. M.; Hu, J. S.; Guo, Y. G.; Zheng, S. F.; Zhong, L. S.; Song, W. G.; Wan, L. J. *Adv. Mater.* **2008**, *20*, 1160.

Characterization. The powder X-ray diffraction (XRD) pattern was recorded on a Rigaku model D/MAX-2500V system (Cu Kα radiation). Scanning electron microscopy (SEM) images were obtained on a JEOL model 6701F electron microscope at 10.0 kV. Transmission electron microscopy (TEM) was performed on a JEOL model 1011F electron microscope that was operating at 100 kV, while high-resolution transmission electron microscopy (HRTEM) was performed using a JEOL model 2010F electron microscope that was operating at 200 kV. The magnetic properties were collected using vibrating sample magnetometry (VSM) at room temperature. Thermogravimetric analysis (TGA) and inductively coupled plasma−optical emission spectroscopy (ICP−OES) was used to reveal the precise chemical composition of the $Fe_3O_4@C$ composite. TGA data were achieved on a Perkin−Elmer model Pyris 1 TGA system. ICP−OES tests were conducted on a Profile-ICP apparatus (Leeman).

Electrochemical properties of the products were measured using Swagelok-type Li^+-ion battery cells. The working electrodes were prepared by casting a slurry that consisted of 80 wt % active material (Fe_3O_4 nanoparticles, $Fe_3O_4@C$ composite, or commercial Fe_3O_4), 10 wt % poly(vinylidene fluoride) (PVDF), and 10 wt % carbon black onto a copper foil. The mass of active powder in each cell is ca. 1.2 mg on a 10-mm-diameter copper foil. A Celgard 2400 microporous polypropylene membrane was used as a separator. The electrolyte consisted of a solution of 1 M $LiPF_6$ in an ethylene carbonate/dimethyl carbonate (EC/DMC) mixture (1:1 v/v). Lithium foils were used as counterelectrodes. These cells were assembled in an argon-filled glovebox and cycled at various rates between voltage limits of 0 V and 3 V.

Results and Discussion

As illustrated by Figure 1, the beaker-in-autoclave setup is designed to confine the synthesis at the liquid/gas interface inside a sealed space. Iron nitrate (Fe^{3+} species) in EG solution was stored in the beaker, while aqueous ammonia solution ($NH_3 \cdot H_2O$) was placed in the autoclave liner outside the beaker. At room temperature, the beaker separates the two solutions. During the reaction, with the assistance of a programmable microwave oven, the system was heated to 170 °C quickly (normally within 1 min) and then kept at that temperature for various times. Such a temperature increase results in the evaporation of ammonia, which reacts with Fe^{3+} at the liquid/gas interface. A black Fe_3O_4 colloidal suspension was formed in the beaker and was collected via centrifugation and ethanol wash cycles. The yield of the Fe_3O_4 against the iron nitrate is almost 100%.

Figure 2 shows TEM images of the Fe_3O_4 nanoparticles. The average diameter of the Fe_3O_4 nanoparticles is ∼6.5 nm after 10 min of reaction time, while the average particle size increases to 9.4 and 11 nm after 1 and 3 h of reaction time, respectively. The size distributions depicted in the insets of Figure 2 also show that the particle size distributions are narrow. Figure 2d is an HRTEM image of a selected nanoparticle from Figure 2c. The shape and the size of the boundary around the parallel crystal lattice fringes suggest that each iron oxide nanoparticle is a single crystal. The lattice plane distance is 2.91 Å, corresponding to the [220] lattice plane of Fe_3O_4 nanoparticles.

XRD patterns of the products produced with different reaction times show that the as-synthesized products were highly crystalline. The diffraction patterns and relative
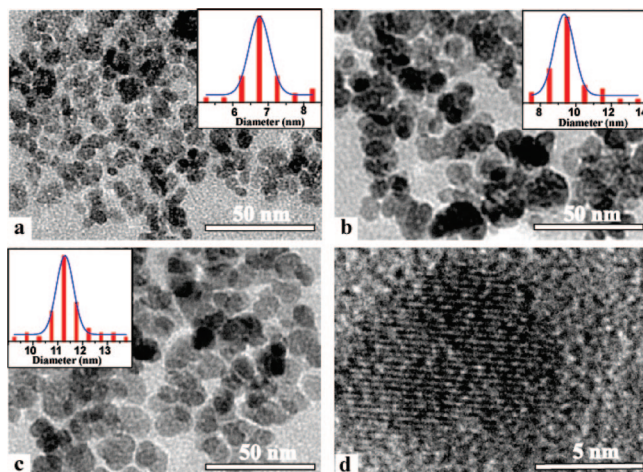
Figure 2. Transmission electron microscopy (TEM) images of the as-synthesized Fe_3O_4 nanocrystals with reaction times of (a) 10 min, (b) 1 h, and (c) 3 h. (Insets show the size distribution of the nanocrystals.) Panel d shows an HRTEM image of a selected particle from panel c.
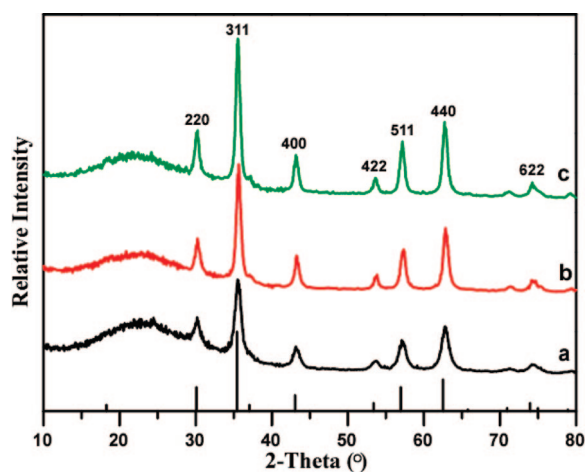

Figure 3. X-ray diffraction (XRD) pattern of the as-synthesized nanocrystals after various reaction times: 10 min (spectrum a), 1 h (spectrum b), and 3 h (spectrum c). The bottom of the image indicates the JCPDS data (JCPDS File Card No. 19-0629) for magnetite.

intensities of all diffraction peaks match well with those of magnetite (Joint Committee on Powder Diffraction Standards (JCPDS) File Card No. 19-0629; see Figure 3). The XRD peak widths and intensities agree very well with the sizes of the Fe_3O_4 nanoparticles, which increases as the reaction time increases.

It has been established that simultaneous nucleation at many sites and the subsequent local crystallization are two crucial factors in synthesizing monodispersed nanoparticles with a narrow size distribution.[27,28] These two factors are realized in the beaker-in-autoclave setup. At elevated temperature, ammonia is evaporated into the sealed space above the EG and $Fe(NO_3)_3$ solution. At the gas/liquid interface, NH_3 reacts with Fe^{3+} to produce $Fe(OH)_3$. Because both NH_3 and Fe^{3+} are all homogeneously distributed at the gas/liquid interface, the formation of $Fe(OH)_3$ is uniform and simultaneous at the interface. Furthermore, the reaction is limited

at the interface, so that the particle growth is localized. During the reaction, the convection inside the beaker will cause the particles to become immersed in the liquid and return back to the interface along the convection flow, which helps to maintain uniform particle sizes.

EG was chosen as the solvent because of its high boiling point and strong polarity, as well as its ability as a reducing agent and capping agent. Deng et al. reported that highly dispersed Fe_3O_4 microspheres were synthesized in EG using polyethylene glycol as a surfactant.[29] In this study, at the reaction temperature (170 °C), $Fe(OH)_3$ is quickly dehydrolyzed to Fe_2O_3 and then is reduced to Fe_3O_4.

In a controlled experiment using water as the solvent in the beaker, we observed red α-Fe_2O_3 aggregates with irregular morphology (shown in Figure S1 in the Supporting Information). This is because NH_3 will be dissolved in the water, causing the uncontrolled precipitation of $Fe(OH)_3$. EG is not a good solvent for NH_3; the reaction between NH_3 and Fe^{3+} was limited at the gas/liquid interface. In addition, EG can bind to the magnetite as the capping agent, helping to preserve the dispersion of Fe_3O_4 particles.

These samples have excellent solubility in water and ethanol. When it was redispersed in water or in ethanol, dark but transparent solutions are obtained. The concentration of the aqueous solution in Figure 1 is 7.0 mg/mL. The dark aqueous solution remains a transparent solution for more than a week before precipitation slowly occurs, while the ethanol solution has yet to show phase separation after four months. The ethanol solution with the Fe_3O_4 nanoparticles can be enriched to a higher concentration (50 mg/mL). Figure 1c shows that, when the concentrated ethanol solution is placed between two poles of a magnet, two identical liquid hills are formed, which are indicative of their magnetic properties.

Gupta et al. reported that Fe_3O_4 nanoparticle single crystals are superparamagnetic when their sizes are below a critical value.[30] To study the magnetic properties of the Fe_3O_4 nanoparticles in this work, the room-temperature magnetization hysteresis curves of the as-synthesized nanocrystals are measured using vibrating sample magnetometry (VSM). The magnetization curves, as shown in Figure 4, display the high saturation magnetizations of three magnetite nanoparticles. The saturation magnetization increases from 39 emμ/g to 55 emμ/g, then to 66 emμ/g with the growth of particle size and enhancement in crystallinity. Furthermore, the forward and backward magnetization curves of 6- and 9-nm Fe_3O_4 samples are almost the same; no hysteresis loops are observed. The inset of Figure 3 shows an expanded view of the curves near the $H = 0$ region, showing that both curves go through the same zero magnetization point at $H = 0$. These data established that both the 6- and 9-nm Fe_3O_4 samples obtained are superparamagnetic nanoparticles. A small hysteresis loop for the 11-nm samples can be observed in the inset shown in Figure 4. This probably indicates that a size of 11 nm is approaching the critical value for Fe_3O_4 nanoparticles to be superparamagnetic, or a small amount

(27) Kwon, S. G.; Piao, Y.; Park, J.; Angappane, S.; Jo, Y.; Hwang, N. M.; Park, J. G.; Hyeon, T. *J. Am. Chem. Soc.* **2007**, *129*, 12571.
(28) Murray, C. B.; Norris, D. J.; Bawendi, M. G. *J. Am. Chem. Soc.* **1993**, *115*, 8706.

(29) Deng, H.; Li, X. L.; Peng, Q.; Wang, X.; Chen, J. P.; Li, Y. D. *Angew. Chem., Int. Ed.* **2005**, *44*, 2782.
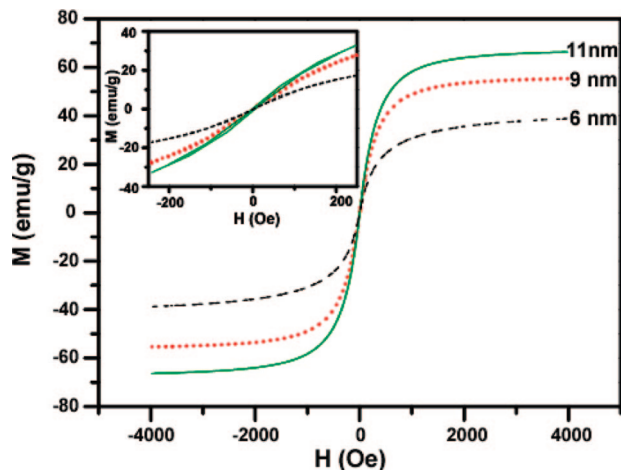(30) Gupta, A. K.; Gupta, M. *Biomaterials* **2005**, *26*, 3995.

Figure 4. Room-temperature hysteresis curves of the as-synthesized Fe_3O_4 products with diameters of 6 nm (dashed line), 9 nm (dotted line), and 11 nm (solid line). Inset shows an enlarged view around the $H = 0$ region.
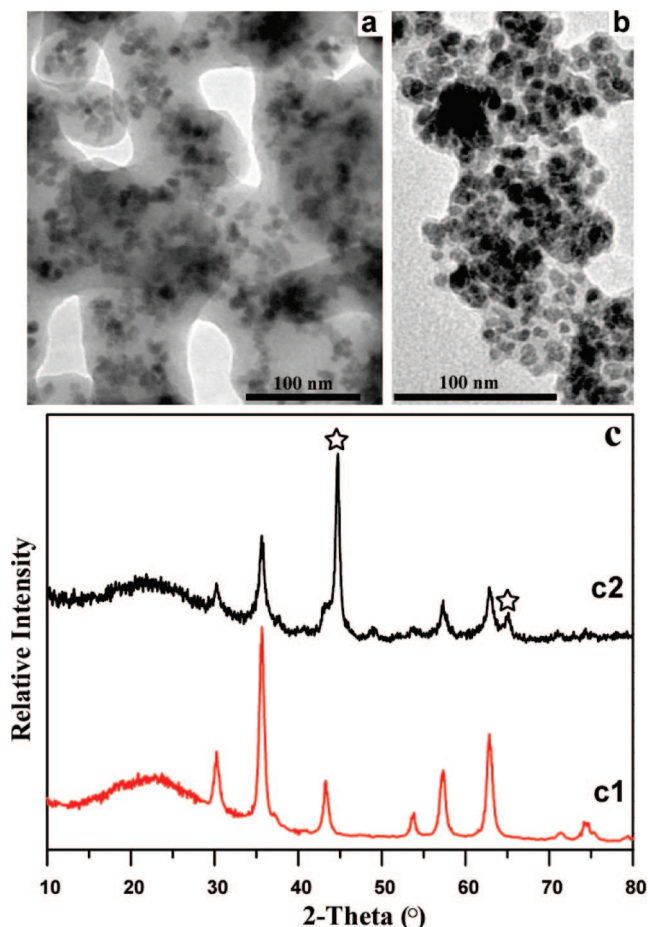

Figure 5. (a) TEM images of (a) an Fe_3O_4@C precursor and (b) an Fe_3O_4@C composite. The XRD patterns shown at the bottom of the image (panel c) show XRD patterns for the Fe_3O_4@C precursor (spectrum c1) and the Fe_3O_4@C composite (spectrum c2). Peaks denoted with an open star (☆) belong to body-centered cubic iron (bcc Fe).

of large-sized Fe_3O_4 crystals is present and causes the hysteresis loop.

Water-soluble and highly dispersed Fe_3O_4 nanocrystals can be readily encapsulated by carbon (see Figure 5a) and silica (see Figure S2 in the Supporting Information), through simple hydrothermal or sol−gel approaches. In a typical carbon encapsulation process, Fe_3O_4 nanocrystals were first dispersed

in the glucose−EtOH/H₂O solution in an autoclave. The autoclave then was sealed and heated to 190 °C and kept at that temperature for 15 h. As the glucose was pyrolyzed to become a carbonaceous matrix, Fe_3O_4 nanocrystals were wrapped into the matrix (Figure 5a). The obtained Fe_3O_4@C precursor was calcined at 600 °C under nitrogen protection for 20 h to form a Fe_3O_4@C composite.

One particular feature of these materials is that Fe_3O_4 nanoparticles remain dispersed inside the carbon matrix. As shown in Figure 5b, the Fe_3O_4 nanoparticles are physically isolated by the carbon matrix, so that the composition is similar to a solid suspension. XRD patterns of the Fe_3O_4@C precursor demonstrated that the Fe_3O_4 nanocrystals inside the carbon precursor matrix did not change their crystal structure (see Figure 5c). However, metallic iron with body-centered cubic (bcc) structures was detected in the Fe_3O_4@C composite, indicating that part of the surface of the Fe_3O_4 nanocrystals was reduced to elemental iron (Fe^0) by the carbon matrix during the calcinations (see Figure 5c). From the TGA and ICP−OES data of the Fe_3O_4@C composite (shown in Figure S4 of the Supporting Information), the amount of metallic iron species is determined to be ∼14.2 wt % of the composite. Such a Fe_3O_4@Fe@C structure may lead to promising applications for these composite materials.

We conducted a preliminary investigation into their electrochemical performance toward lithium uptake−release, and we compared its performance with that of bare Fe_3O_4 nanocrystals and commercial Fe_3O_4 particles (Alfa Aesar, ∼300 nm in diameter). The results are shown in Figure 6a, in which a rate of C/10 (8 Li per Fe_3O_4 in 10 h) has been used. In the first cycle, the charge capacity of the commercial Fe_3O_4 particles is ∼800 mA h/g. However, its capacity continuously decreases and reaches 201 mA h/g after 30 cycles, indicating poor capacity retention. Bare Fe_3O_4 nanocrystals have even worse capacity-retention properties than the commercial Fe_3O_4. After 30 cycles, its capacity is only 70 mA h/g. The high surface area of bare Fe_3O_4 nanoparticles raises the risk of secondary reactions involving electrolyte decomposition between the electrode and the electrolyte, which should be the main reason for the poor cycling performance.[31] In sharp contrast, the reversible capacity of the Fe_3O_4@C composite is constantly above 600 mA h/g, which is much higher than that of the conventional graphite anode (LiC_6, 372 mA h/g), showing excellent retention of capacity on cycling. Note that the mass of carbon is included when calculating the specific reversible capacity of the Fe_3O_4@C composite.

In addition to the much improved cycling performance, the Fe_3O_4@C composite also shows significantly enhanced rate performance, compared to that of the commercial Fe_3O_4 particles (Figure 6b). At a high rate of 5C (discharge/charge of all active materials within 12 min), the reversible capacity of Fe_3O_4@C composites is 173 mA h/g, whereas the commercial Fe_3O_4 particles have no capacity under this condition. The results indicate that dispersing Fe_3O_4 nanoparticles into a carbon matrix is an effective way to improve both the

(31) Okubo, M.; Hosono, E.; Kim, J.; Enomoto, M.; Kojima, N.; Kudo, T.; Zhou, H. S.; Honma, I. *J. Am. Chem. Soc.* **2007**, *129*, 7444.
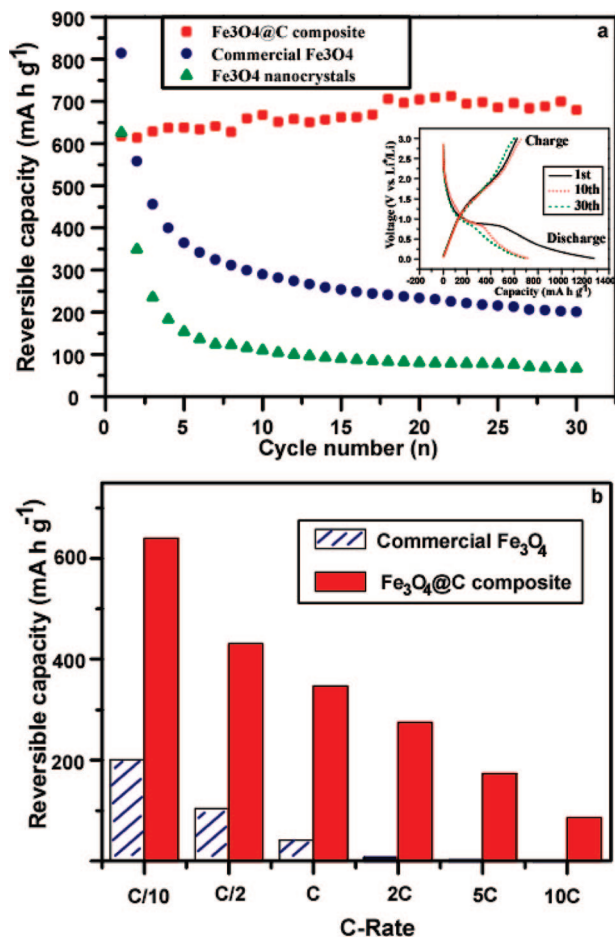
Figure 6. (a) Variation in reversible capacity versus cycle number for the Fe_3O_4@C composite, commercial Fe_3O_4 particles, and Fe_3O_4 nanocrystals at a rate of C/10. Inset shows the 1st, 10th, and 30th discharge/charge voltage profiles of the Fe_3O_4@C composite at a rate of C/10. (b) Rate performances for the Fe_3O_4@C composite and commercial Fe_3O_4 particles.

cycling performance and rate performance of Fe_3O_4-based anode materials.

The improvement is attributed to the following three factors. First, the surface of the nanosized Fe_3O_4 particles was reduced to metallic iron, which does not contribute to charge capacity but may enhance the electron-conducting network, as well as the surface electrochemical reactivity.[19] Second, nanosized Fe_3O_4 particles dispersed in a carbon matrix reduces the diffusion courses of the Li^+ ions. Both of these two factors are advantageous for the kinetics toward Li uptake−release. This is the key to the excellent rate (power) performance. Last, during Li uptake, Fe_3O_4 is

converted to Fe^0 and Li_2O, resulting in a volume expansion of ~180%, which leads to gradual lattice destruction and deteriorating performance of normal Fe_3O_4. In the Fe_3O_4@C composite, however, Fe_3O_4 nanoparticles are physically isolated by the carbon matrix; any physical change of one Fe_3O_4 nanoparticle is restricted at its local region. The carbon matrix may also acts as an elastic buffer to relieve the strain associated with the volume variations during Li uptake− release cycles, leading to excellent cycling performance. A similar result was reported by Scrosati et al. on the Sn@C system.[32] In addition, the XRD pattern and TEM image of the Fe_3O_4@C composite used each show that the crystalline nature and morphology of the Fe_3O_4 nanoparticle remain almost unchanged, in comparison to the original composite (see Figures S5 and S6 in the Supporting Information), again suggesting that such a composite structure indeed helps to maintain a stable structure of the anode materials.

Conclusion

In summary, highly dispersed magnetite nanocrystals were produced by limiting the reaction at the gas/liquid interface. This is achieved through the use of a "beaker-in-autoclave" setup. The magnetite nanocrystals have uniform and controllable sizes and are soluble in water. Fe_3O_4 nanocrystals can be easily encapsulated in carbon to form a Fe_3O_4@C composite, which is a promising anode material for high-performance lithium-ion batteries.

Supporting Information Available: SEM image of the product from control experiment (Figure S1); SEM (A) and TEM (B) image of the highly disperse nanocrystal encapsulated in silica (Figure S2); TG trace of the as-synthesized Fe_3O_4@C precursor (Figure S3) and TG trace of the Fe_3O_4@C composite (Figure S4); XRD image of the postused Fe_3O_4@C composite in lithium batteries (Figure S5); and TEM image of the postused Fe_3O_4@C composite in lithium batteries. (PDF) This material is available free of charge via the Internet at http://pubs.acs.org.

CM8033609

(32) Derrien, G.; Hassoun, J.; Panero, S.; Scrosati, B. *Adv. Mater.* **2007**, *19*, 2336.